Analysis of coding metasurfaces for incident radiation at oblique incidence angles

JAN KAPPA,* ZINCHING DANG, DOMINIK SOKOLUK, AND MARCO RAHM

Department of Electrical and Computer Engineering and Research Center OPTIMAS, Technische Universität Kaiserslautern, Kaiserslautern, Germany
*kappa@eit.uni-kl.de

Abstract: Radar cross section reducing (RCSR) metasurfaces or coding metasurfaces were primarily designed for normally incident radiation in the past. It is evident that the performance of coding metasurfaces for RCSR can be significantly improved by additional backscattering reduction of obliquely incident radiation, which requires a valid analytic conception tool. Here, we derive an analytic current density distribution model for the calculation of the backscatter far-field of obliquely incident radiation on a coding metasurface for RCSR. For demonstration, we devise and fabricate a metasurface for a working frequency of 10.66 GHz and obtain good agreement between the measured, simulated, and analytically calculated backscatter far-fields. The metasurface significantly reduces backscattering for incidence angles between −40° and 40° in a spectral working range of approximately 1 GHz.

1. Introduction

Over the last years, researchers have focused on the design and analysis of metamaterials as engineered composite materials that offer configurable electromagnetic properties beyond the frontiers determined by nature [1]. Especially the non-bulky, two-dimensional representation of a metamaterial, the metasurface, has gained a lot of attention. With its comparably easy manufacturability and flexibility, it is ideally suited as a material for radar cross section reduction (RCSR) to hide objects from detection by radar systems.

The corresponding design of a metasurface for RCSR relies on a proper geometry and composition of artificial magnetic conductors and electric conductors as unit cells. Combined in a checkerboard pattern, a metasurface can spread the backscattered far field of the incident radiation into 4 main lobes [2], which consequently reduces the radar cross section in the specular direction. In 2014, Cui et al. introduced a new design approach for RCSR metasurfaces by using coding, digital or programmable elements as unit cells [3] that allow adequate control of the phase response of every single cell. By combining two unit cells that backscatter incident radiation with a relative phase difference of 180°, they were able to implement a 1-bit coding metasurface for RCSR. Since such a RCSR metasurface can be considered as a surface with encoded digital spatial phase pattern, it naturally links to the field of information theory and signal processing [4–6]. This analogy sparked the idea to include generic algorithms combined with numeric simulations as a method for the design of coding metasurfaces [7–12] and led to the realization of multi-bit coding metasurfaces [13]. In this context, Cui et al. provided an analytic model that allows the computation of the backscatter far-field by considering the coding metasurface as a passive antenna array [3]. This approach was used and step-wise improved in recent years [14–16]. Yet, the calculations have only accounted for backscattering of waves that were normally incident on the metasurface. So far, the literature lacks of a closed analysis that allows computation of the backscatter far-field after oblique incidence on a coding metasurface or seems misleading [17,18]. Recent publications report the successful design and realization of a

broadband and broad angle coding metasurface under oblique incidence angles, while calculating the well known case of normal incidence [11,19–22].

Here, we provide a closed analytic model that enables the calculation of the backscatter far-field of a coding metasurface for waves at arbitrary oblique incidence angles. We show that the approach is a proper means for the fast conception of coding metasurfaces and apply the method to design a coding metasurface for RCSR that suppresses backscattering for obliquely incident waves. In order to corroborate the appropriateness of the analytic model, we fabricated the devised coding metasurface for RCSR for a working frequency of 10.66 GHz and measured the backscatter field by use of a microwave goniometer. A comparison between the measured and analytically computed backscatter field showed good agreement. As a further validation, we numerically calculated the backscatter field in a 3-D full wave simulation, which was also in good agreement with the results obtained by the analytic calculation.

2.   Analytic description

In analogy to [5], we consider a coding metasurface as an antenna array, whose spatial far-field distribution $\vec{f}(\vec{r})$ can be determined by knowledge of the macroscopic current density distribution $\vec{J}(\vec{r})$ in the antenna structure. In a scalar consideration, we can exploit the proportionality of the far-field $f(\vec{r})$ to the magnitude of the relevant component of the magnetic vector potential $A(\vec{r})$ for calculation of $f(\vec{r})$ under Lorentz gauge by

$$f(\vec{r}) = \int_V J(\vec{r}') \, \exp\left(-\mathrm{j}k\frac{\vec{r}}{|\vec{r}|} \cdot \vec{r}'\right) \mathrm{d}V' \propto A(\vec{r}) \quad , \text{ with } \vec{r} = (x, y, z)^T \tag{1}$$

In Eq. (1), $\vec{r}'$ determines the location of the current density, whereas $\vec{r}$ describes an arbitrary observation point in the far field. The magnitude of the wave vector of the emitted wave is denoted as $k = \frac{2\pi}{\lambda}$, where λ is the wavelength of the wave.

For the analysis of the backscattering of electromagnetic radiation from a coding metasurface, we subdivide the surface into coding elements that are indexed by the row number m and the column number n. In each coding element, we assume a complex point current with current density $J_{m,n}(\vec{r}')$ in the center point $(x' - (m - \frac{1}{2}), y' - (n - \frac{1}{2}), 0)$ of the $(m, n)^{\text{th}}$ coding element, according to Fig. 1. With $\vec{k}_r$ being the wave vector of the backscattered electromagnetic wave and under the assumption of a constant point current amplitude I_0, we obtain

$$J_{m,n}(\vec{r}') = I_0 \, \exp\left(\mathrm{j}\varphi_{m,n} + \mathrm{j}\vec{k}_r \cdot \vec{r}'\right) \delta\left(x' - \left(m - \frac{1}{2}\right)D_x\right) \delta\left(y' - \left(n - \frac{1}{2}\right)D_y\right) \delta(z') \tag{2}$$

Hereby, $\varphi_{m,n}$ denotes the initial phase of the point current density in the $(m, n)^{\text{th}}$ coding element and the functional δ symbolizes the one-dimensional, spatial delta distribution.

In a first step, we calculate the far-field distribution of the backscattered wave from the coding metasurface after normal incidence in order to compare the results with existing work reported in [3–5]. In this case, the wave vector of the backscattered light must obey the condition $\vec{k}_r = -\vec{k}_i = k\vec{e}_z$ in Eq. (2), where $\vec{k}_i$ represents the wave vector of the incident wave and $\vec{e}_z$ denotes the unit normal vector to the metasurface, according to Fig. 1. By inserting Eq. (2) in Eq. (1), we obtain for the far field distribution of the $(m, n)^{\text{th}}$ coding element

$$f_{m,n}(\vec{r}) = \int_V J_{m,n}(\vec{r}') \, \exp\left(-\mathrm{j}k\frac{\vec{r}}{|\vec{r}|} \cdot \vec{r}'\right) \mathrm{d}V' \tag{3}$$
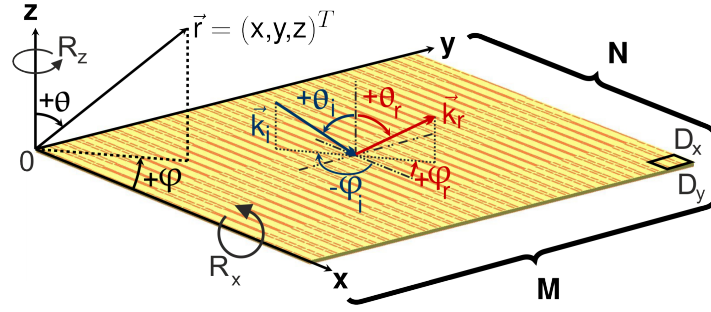
Fig. 1. Coordinate system and relevant variables for the calculation of the backscatter far-field of a coding metasurface for RCSR with $M \times N$ unit cells. Each unit cell has a length D_x and a width D_y. R_x and R_z indicate rotation around the x- and z-axis, respectively. The signs of the incidence and reflection angles are indicated as used in the calculations. Variables attributed to incident waves are indexed by i, the quantities of backscattered waves are indexed by r. Spherical coordinates are described by a vector (r, θ, φ).

$$= \int_V I_0 \, \exp\left(\mathrm{j}\varphi_{m,n} + \mathrm{j}\vec{k}_r \cdot \vec{r}' - \mathrm{j}k\frac{\vec{r}}{|\vec{r}|} \cdot \vec{r}'\right) \delta\left(x' - \left(m - \frac{1}{2}\right)D_x\right)$$

$$\delta\left(y' - \left(n - \frac{1}{2}\right)D_y\right) \delta(z') \, \mathrm{d}V' \tag{4}$$

In cartesian coordinates, $f_{m,n}(\vec{r})$ can be determined as

$$f_{m,n}(\vec{r}) = \int_V I_0 \exp\left(\mathrm{j}\varphi_{m,n} + \mathrm{j}k\left(z' - \frac{xx' + yy' + zz'}{\sqrt{x^2 + y^2 + z^2}}\right)\right) \delta\left(x' - \left(m - \frac{1}{2}\right)D_x\right)$$

$$\delta\left(y' - \left(n - \frac{1}{2}\right)D_y\right) \delta(z') \, \mathrm{d}V' \tag{5}$$

$$= I_0 \exp\left(\mathrm{j}\left[\varphi_{m,n} - k\frac{x}{\sqrt{x^2 + y^2 + z^2}}\left(m - \frac{1}{2}\right)D_x - k\frac{y}{\sqrt{x^2 + y^2 + z^2}}\left(n - \frac{1}{2}\right)D_y\right]\right) \tag{6}$$

Transformation of Eq. (6) to spherical coordinates and summation over all $M \times N$ coding elements yields the far field distribution

$$f(\theta, \varphi) = \sum_{m=1}^{M} \sum_{n=1}^{N} f_{m,n}(\vec{r}) \tag{7}$$

$$= \sum_{m=1}^{M} \sum_{n=1}^{N} \exp\left(\mathrm{j}\left[\varphi_{m,n} - k\frac{|\vec{r}|\sin(\theta)\cos(\varphi)}{|\vec{r}|}\left(m - \frac{1}{2}\right)D_x - k\frac{|\vec{r}|\sin(\theta)\sin(\varphi)}{|\vec{r}|}\left(n - \frac{1}{2}\right)D_y\right]\right) \tag{8}$$

$$= \sum_{m=1}^{M} \sum_{n=1}^{N} \exp\left(\mathrm{j}\left[\varphi_{m,n} - kD_x\left(m - \frac{1}{2}\right)\sin(\theta)\cos(\varphi) - kD_y\left(n - \frac{1}{2}\right)\sin(\theta)\sin(\varphi)\right]\right), \tag{9}$$

similar to the findings in [3–5].

Based on Eq. (4) and the validity of the reflection law, it is straightforward to calculate the reflection from a metasurface for incident waves at arbitrary, oblique incidence angles (θ_i, φ_i). By

application of rotation matrices, the wave vector $k_i(\theta_i, \varphi_i)$ of the incident wave can be construed from the wave vector $\vec{k}_{i,\perp} = k_{i,\perp}(0, 0, -1)^T$ for normal incidence by

$$\vec{k}_i = R_z(\varphi_i + 90°) \cdot R_x(\theta_i) \cdot k_{i,\perp}(0, 0, -1)^T = k_{i,\perp}(-\sin(\theta_i)\cos(\varphi_i), -\sin(\theta_i)\sin(\varphi_i), -\cos(\theta_i))^T$$
(10)

Here, R_z and R_x denote the rotation matrix around the z- and x-axis according to Fig. 1.

In compliance with the reflection law, the wave vector of the reflected wave must obey

$$\vec{k}_r = R_z(\varphi_i - 90°) \cdot R_x(\theta_i) \cdot k_{i,\perp}(0, 0, 1)^T = k_{i,\perp}(-\sin(\theta_i)\cos(\varphi_i), -\sin(\theta_i)\sin(\varphi_i), \cos(\theta_i))^T \quad (11)$$

Inserting Eq. (11) in Eq. (4) delivers for the far-field distribution of a single coding element for oblique incidence in cartesian coordinates.

$$f_{m,n}(\vec{r}) = \int_V I_0 \exp\left(j\varphi_{m,n} + jk(-x'\sin(\theta_i)\cos(\varphi_i) - y'\sin(\theta_i)\sin(\varphi_i) + z'\cos(\theta_i))\right.$$

$$\left. + jk\left(z' - \frac{xx' + yy' + zz'}{\sqrt{x^2 + y^2 + z^2}}\right)\right)\delta\left(x' - \left(m - \frac{1}{2}\right)D_x\right)\delta\left(y' - \left(n - \frac{1}{2}\right)D_y\right)\delta(z')\,dV'$$
(12)

$$= I_0 \exp\left(j\left[\varphi_{m,n} - k\left(m - \frac{1}{2}\right)D_x\sin(\theta_i)\cos(\varphi_i) - k\left(n - \frac{1}{2}\right)D_y\sin(\theta_i)\sin(\varphi_i)\right.\right.$$

$$\left.\left. - k\frac{x}{\sqrt{x^2 + y^2 + z^2}}\left(m - \frac{1}{2}\right)D_x - k\frac{y}{\sqrt{x^2 + y^2 + z^2}}\left(n - \frac{1}{2}\right)D_y\right]\right)$$
(13)

After summation over all $M \times N$ coding elements and transformation of Eq. (14) to spherical coordinates, we obtain the incidence-angle-dependent far-field distribution of backscattered radiation from the coding metasurface as

$$f(\theta, \varphi) = \sum_{m=1}^{M}\sum_{n=1}^{N}\exp\left(j\left(\varphi_{m,n} - kD_x\left(m - \frac{1}{2}\right)[\sin(\theta)\cos(\varphi) + \sin(\theta_i)\cos(\varphi_i)]\right.\right.$$

$$\left.\left. - kD_y\left(n - \frac{1}{2}\right)[\sin(\theta)\sin(\varphi) + \sin(\theta_i)\sin(\varphi_i)]\right)\right)$$
(14)

For a flat uncoded surface, i.e. $\varphi_{m,n} = 0$ for all (m, n), $f(\theta, \varphi)$ correctly describes the reflected far-field from the flat surface after oblique incidence, in compliance with the reflection law.

3. Numerical simulation

Our goal was the design and implementation of a coding metasurface with radar cross section reduction (RCSR) for obliquely incident microwaves as a proof of our analytic description. According to Eq. (14), specular backscattering can be suppressed, if pairs of unit cells reflect waves with a relative phase shift of $\varphi_{m,n} - \varphi_{m',n'} = \pi$, where a unit cell pair consists of the $(m, n)^{th}$ and $(m', n')^{th}$ unit cell. As can be seen in Fig. 3 for the example of incident waves at an incidence angle of $(\theta_i = +40°, \varphi_i = -90°)$, the specular reflection is significantly attenuated for such a metasurface, as the incident wave is predominantly scattered into higher diffraction orders.

For the physical implementation of a coding metasurface for RCSR, we resorted to cut-wire unit cells and numerically calculated the amplitude and phase of the backscattered wave dependent on the wavelength and incidence angle. Due to the specific geometry of the cut-wire design, the metasurface only reduces the scattering cross section for incident waves with an electric field polarization parallel to the cut-wires and a wave vector in the yz-plane. The polarization sensitivity of our design allowed the evaluation of oblique incidence angles, hence the cut-wires

resonantly respond to the electric field. Consequently, the influence of linear polarized radiation at different incident angles on the electric coupling is reduced. The electric field will always proceed parallel to the cut-wires. In addition, it was necessary to combine cut-wire pairs of different lengths to expand the frequency working range of the coding metasurface for RCSR. In order to keep the demands for manufacturability at a minimum, we designed the metasurface for the microwave X band from 8 GHz to 12 GHz. For the numerical calculations, we used CST Microwave Studio 2018©.

The unit cell structure is shown in Fig. 2(a). The square unit cell has a side length of $p = 6$ mm and consists of a copper wire pair on a FR-4 substrate with a copper ground plane on the bottom side. Both copper wires in a cell have a thickness $t_{wire} = 18 \mu$m, a width $w = 0.6$ mm and a length a. The separation between the wires is identical to their length. The thickness of the substrate is $t_{diel} = 1.5$ mm. The copper wires resonantly backscatter incident waves with an electric field polarization parallel to the wires. By variation of the wire length a, the resonance frequency and thus the amplitude and phase of the backscattered waves can be designed at will. By this means, it is possible to devise unit cell pairs that reflect incident waves with identical amplitude, but a mutual phase difference of 180°. Due to destructive interference between the reflected waves, specular
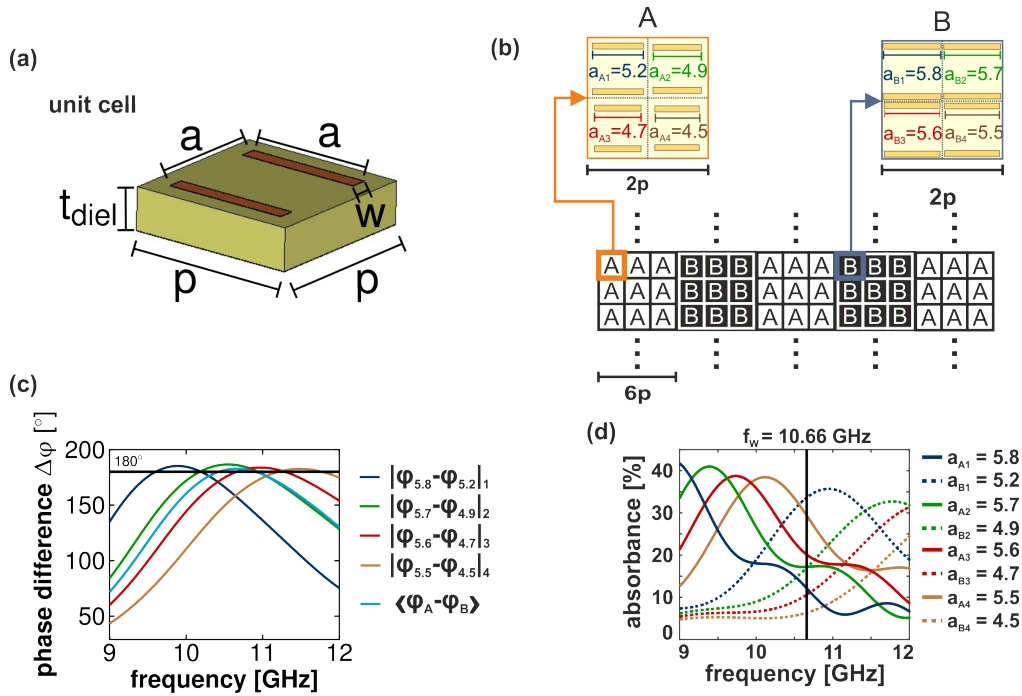

Fig. 2. (a) Cut wire unit cell of the coding metasurface for RCSR with p: unit cell side length, a: cut wire length and distance, w: cut wire width, t: cut wire thickness, and t_{diel}: substrate thickness. (b) Alternating arrangement of the unit cells in regions A and B as rows of width $6p$. Each unit cell in region A pairs with a unit cell in region B. The four unit cell pairs, that are resonant at 4 neighboring frequencies, reflect incident waves with a phase difference of 180° in their individual frequency working range. (c) Frequency dependence of the relative phase shift $|\varphi_{a_{Ai}} - \varphi_{a_{Bi}}|_i$ of the ith unit cell pair calculated based on the numeric simulation results for the phase of the reflected electromagnetic waves of each unit cell. (d) Dependence of the spectral unit cell absorption on the cut wire length , where the solid and dashed lines of the same color correspond to a unit cell pair whose phase difference was plotted in (c).

reflection is reduced to a minimum while backscattering in higher diffraction orders is allowed. To broaden the spectral working range of the coding metasurface for RCSR, we combined four unit cell pairs that resonantly minimize specular reflection at four different resonance frequencies (see Fig. 2(c)). Each unit cell in region A pairs with another unit cell in region B. The corresponding unit cell pairs reflect incident waves with a relative phase difference of 180° at their respective working frequency. In Fig. 2(b), unit cell pairs are labeled by text and numbers of the same color. As can be seen, the spatial position of regions A and B alternates periodically with a spatial period length of $6p$. Figure 2(c) depicts the frequency dependence of the phase difference between reflected waves from the two unit cells within a unit cell pair. Unit cell pairs with wire length combinations $(a_{A1} = 5.2, a_{B1} = 5.8)_1, (a_{A2} = 4.9, a_{B2} = 5.7)_2, (a_{A3} = 4.7, a_{B3} = 5.6)_3$ and $(a_{A4} = 4.5, a_{B4} = 5.5)_4$ are considered, as indicated in Fig. 2 (b). The corresponding phase difference is denoted as $|\varphi_{a_{A_i}} - \varphi_{a_{B_i}}|_i$, where a_{A_i} and a_{B_i} are the cute wire length in the ith unit cell in region A and B, respectively. It is obvious that the four unit cell pairs are designed for neighboring working frequencies (see Fig. 2(c)). We define the working frequency of a unit cell pair as the frequency, for which the phase difference of the reflected waves $|\varphi_{A_i} - \varphi_{B_i}|_i$ in the ith unit cell is approximately 180°. The corresponding frequency working range is defined as the frequency interval, in which the phase difference remains at this value within an accuracy of ±2°. The observed frequency working range is typically of the order of 100 MHz (compare Fig. 2(c)). Due to the proximity of the working frequencies of the unit cell pairs, specular reflection from the metasurface can be efficiently suppressed over a frequency working range of 860 MHz around a working frequency of $f_w = 10.66$ GHz, indicated by the light blue curve in Fig. 2(c) with the label $\langle \varphi_A - \varphi_B \rangle$. We observe that the effective frequency working range of the coding metasurface for RCSR is successfully broadened by combination of four unit cell pairs with different working frequencies, compared to the working range of an individual unit cell pair. In addition, the combination of unit cell pairs with different resonance frequencies makes the coding metasurface for RCSR robust against fabrication tolerances.

We also investigated the spectral absorbance of electromagnetic waves in each of the unit cells, which is illustrated in Fig. 2(d). The absorption in unit cells of the same unit cell pair are plotted in the same color, one as solid line and the other as dashed line. We note that none of the unit cells possesses its absorbance maximum at the effective resonance frequency of the combined structure, which is at 10.66 GHz. Furthermore, the transmission through the metasurface is basically zero due to the metallic ground plane. For this reason, we can conclude that the specular reflection is mainly reduced by destructive interference rather than by absorption, which requires proper amplitude and phase engineering of the coding metasurface for RCSR.

In a next step, we numerically calculated the electromagnetic backscatter far-field of the coding metasurface for the example of an incident wave at an angle of $\theta_i = +40°$ with respect to the z-axis and an angle of $\varphi_i = -90°$ to the x-axis. The electric field polarization is in x-direction parallel to the wires. A comparison between the analytically and numerically calculated backscatter far-fields, displayed in Figs. 3(a) and (b), indicate excellent agreement between the analytic and numerical calculation. Both calculations evidence that the fields are scattered at a reflection angle $\theta_r = \theta_i$, yet are mainly diffracted into two side lobes away from the direction of specular reflection, which is expected for a reflection angle $\varphi_r = \varphi_i + 180° = 90°$. This observation confirms a strong reduction of specular reflection from the coding metasurface for RCSR and thus verifies the applicability of the analytic model for the proper design of coding metasurfaces for obliquely incident radiation.
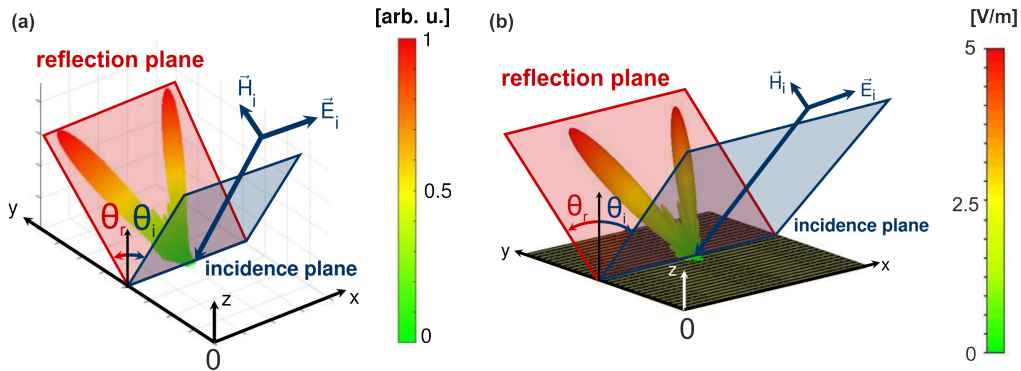
Fig. 3. (a) Analytically and (b) numerically calculated electric backscatter far-field of the designed coding metasurface for oblique incidence at 40°. The incidence and reflection plane are highlighted for visual orientation.

4.   Experimental evaluation

For a further proof of our analytic model, we fabricated the analyzed and simulated coding metasurface for RCSR and measured the backscatter far-field for incident microwaves at angles of $\theta_i = +10°, +20°$ and $+40°$ with respect to the z-axis and a constant angle of $\varphi_i = -90°$ to the x-axis. The microwave frequency was 10.66 GHz. Figure 4(a) shows a photograph of the fabricated metasurface. For the measurement of the far-field distribution, we used a microwave goniometer, as illustrated in Fig. 4(b).
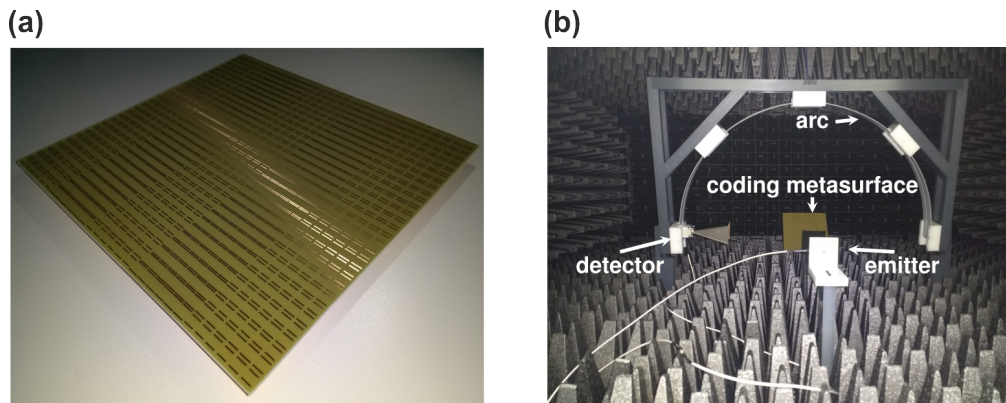

Fig. 4. (a) Photograph of the fabricated metasurface. (b) Photograph of the microwave goniometer with the mounted metasurface.

The measured backscatter far-fields from the metasurface for the three different incidence angles of $\theta_i = +10°, +20°$ and $+40°$ with corresponding $\varphi_i = -90°$ are plotted in the polar diagrams of Figs. 5(a) to 5(c). The polar diagrams also contain the analytically and numerically calculated backscatter fields. For normalization, we also calculated and measured the specular reflection from a flat metal mirror of equal size for the different incidence angles and normalized the backscatter far-fields from the coding metasurface for RCSR to the maximum electric field of the specular reflection from the metal mirror.

The polar diagrams of the far-fields of the coding metasurface for RCSR in Figs. 5(a) to 5(c) reveal predominant backscattering into two side lobes in the corresponding reflection plane at

$\theta_r = +10°, +20°$ and $+40°$ with respect to the z-axis and a constant $\varphi_r = +90°$ to the x-axis . For incidence angles of $\theta_i = +20°$ and $+40°$, the direction and shape of the measured and analytically and numerically calculated side lobes agree well. For an incidence angle of $\theta_i = +10°$, the measured side lobes are distorted due to additional scattering by the mount of the metasurface at this lower incidence angle. In addition, the angular resolution of the measurement was limited to $2.3°$ due to the aperture of the detecting horn antenna. Because of the spatial averaging, we observed a broadening of the side lobe.
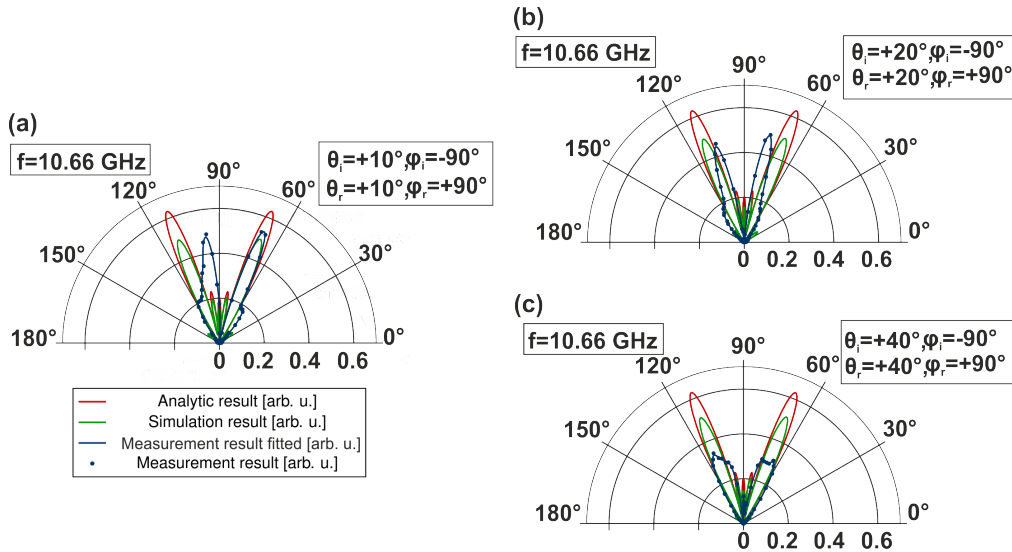
Fig. 5. Comparison between the analytically calculated, numerically calculated and experimentally measured backscatter far-field of the coding metasurface for an incidence angle (a) $(\theta_i = +10°, \varphi = -90°)$, (b) $(\theta_i = +20°, \varphi = -90°)$, and (c) $(\theta_i = +40°, \varphi = -90°)$. The working frequency was $f = 10.66$ GHz.

A comparison between the measured maximum field amplitude of the backscattered electric field and the calculated amplitude reveals the negligence of any absorption in the analytic model of the coding metasurface for RCSR. As a consequence, the amplitude of the analytically calculated backscatter field is higher than the measured amplitude. Regarding the numerical calculations, for which absorption was taken into account, the measured backscatter field amplitudes are in good agreement for incidence angles of $\theta_i = +10°$ and $+20°$. For an incidence angle of $\theta_i = +40°$ in Fig. 5(c), the measured and numerically calculated field amplitudes deviate due to insufficient alignment accuracy of the goniometer. Nevertheless, the measurement of the backscatter far-fields provides further evidence of the applicability of the analytic model for the design of coding metasurfaces for obliquely incident radiation.

5. Conclusion

We theoretically and experimentally analyzed the backscatter properties of a coding metasurface for obliquely incident radiation. For this purpose, we developed an analytic current density distribution model that adequately describes the backscatter far-field distribution of a coding metasurface for RCSR. In order to verify the applicability of the analytic model, we designed and fabricated a coding metasurface for a working frequency of 10.66 GHz and demonstrated good agreement between the measured backscatter far-field and the obtained far-fields from both analytic and numerical calculations. The analytic model enables faster and easier conception of coding metasurfaces for radiation at arbitrary oblique incidence angles.

References

1. D. R. Smith, S. Schultz, P. Markoš, and C. M. Soukoulis, "Determination of effective permittivity and permeability of metamaterials from reflection and transmission coefficients," Phys. Rev. B **65**(19), 195104 (2002).
2. M. Paquay, J. Iriarte, I. Ederra, R. Gonzalo, and P. de Maagt, "Thin amc structure for radar cross-section reduction," IEEE Trans. Antennas Propag. **55**(12), 3630–3638 (2007).
3. T. J. Cui, M. Q. Qi, X. Wan, J. Zhao, and Q. Cheng, "Coding metamaterials, digital metamaterials and programmable metamaterials," Light: Sci. Appl. **3**(10), e218 (2014).
4. T. J. Cui, S. Liu, and L. Zhang, "Information metamaterials and metasurfaces," J. Mater. Chem. C **5**(15), 3644–3668 (2017).
5. T.-J. Cui, S. Liu, and L.-L. Li, "Information entropy of coding metasurface," Light: Sci. Appl. **5**(11), e16172 (2016).
6. S. Liu, T. J. Cui, L. Zhang, Q. Xu, Q. Wang, X. Wan, J. Q. Gu, W. X. Tang, M. Qing Qi, J. G. Han, W. L. Zhang, X. Y. Zhou, and Q. Cheng, "Convolution operations on coding metasurface to reach flexible and continuous controls of terahertz beams," Adv. Sci. **3**(10), 1600156 (2016).
7. Y. Zhao, X. Cao, J. Gao, Y. Sun, H. Yang, X. Liu, Y. Zhou, T. Han, and W. Chen, "Broadband diffusion metasurface based on a single anisotropic element and optimized by the simulated annealing algorithm," Sci. Rep. **6**(1), 23896 (2016).
8. S. J. Li, X. Y. Cao, L. M. Xu, L. J. Zhou, H. H. Yang, J. F. Han, Z. Zhang, D. Zhang, X. Liu, C. Zhang, Y. J. Zheng, and Y. Zhao, "Ultra-broadband reflective metamaterial with rcs reduction based on polarization convertor, information entropy theory and genetic optimization algorithm," Sci. Rep. **6**(1), 37409 (2016).
9. H. Sun, C. Gu, X. Chen, Z. Li, L. Liu, B. Xu, and Z. Zhou, "Broadband and broad-angle polarization-independent metasurface for radar cross section reduction," Sci. Rep. **7**(1), 40782 (2017).
10. Q. Zhang, X. Wan, S. Liu, J. Yuan Yin, L. Zhang, and T. Jun Cui, "Shaping electromagnetic waves using software-automatically-designed metasurfaces," Sci. Rep. **7**(1), 3588 (2017).
11. M. Moccia, S. Liu, R. Y. Wu, G. Castaldi, A. Andreone, T. J. Cui, and V. Galdi, "Coding metasurfaces for diffuse scattering: Scaling laws, bounds, and suboptimal design," Adv. Opt. Mater. **5**(19), 1700455 (2017).
12. L. Bai, X. G. Zhang, S. H. Bal, and W. X. Jiang, "Broadband coding metasurface for radar cross section reduction," in *2018 Cross Strait Quad-Regional Radio Science and Wireless Technology Conference (CSQRWC)*, (2018), pp. 1–3.
13. L.-H. Gao, Q. Cheng, J. Yang, S.-J. Ma, J. Zhao, S. Liu, H.-B. Chen, Q. He, W.-X. Jiang, H.-F. Ma, Q.-Y. Wen, L.-J. Liang, B.-B. Jin, W.-W. Liu, L. Zhou, J.-Q. Yao, P.-H. Wu, and T.-J. Cui, "Broadband diffusion of terahertz waves by multi-bit coding metasurfaces," Light: Sci. Appl. **4**(9), e324 (2015).
14. X. Yan, L. Liang, J. Yang, W. Liu, X. Ding, D. Xu, Y. Zhang, T. Cui, and J. Yao, "Broadband, wide-angle, low-scattering terahertz wave by a flexible 2-bit coding metasurface," Opt. Express **23**(22), 29128–29137 (2015).
15. L. Liang, M. Wei, X. Yan, D. Wei, D. Liang, J. Han, X. Ding, G. Zhang, and J. Yao, "Broadband and wide-angle rcs reduction using a 2-bit coding ultrathin metasurface at terahertz frequencies," Sci. Rep. **6**(1), 39252 (2016).
16. Y. Zhang, L. Liang, J. Yang, Y. Feng, B. Zhu, J. Zhao, T. Jiang, B. Jin, and W. Liu, "Broadband diffuse terahertz wave scattering by flexible metasurface with randomized phase distribution," Sci. Rep. **6**(1), 26875 (2016).
17. Y. Zhou, X. y. Cao, J. Gao, S. Li, and X. Liu, "Rcs reduction for grazing incidence based on coding metasurface," Electron. Lett. **53**(20), 1381–1383 (2017).
18. Q. Zheng, Y. Li, J. Zhang, H. Ma, J. Wang, Y. Pang, Y. Han, S. Sui, Y. Shen, H. Chen, and S. Qu, "Wideband, wide-angle coding phase gradient metasurfaces based on pancharatnam-berry phase," Sci. Rep. **7**(1), 43543 (2017).
19. X. Liu, J. Gao, L. Xu, X. Cao, Y. Zhao, and S. Li, "A coding diffuse metasurface for rcs reduction," IEEE Antennas Wirel. Propag. Lett. **16**, 724–727 (2017).
20. S. Liu, T. Jun Cui, A. Noor, Z. Tao, H. Chi Zhang, G. Dong Bai, Y. Yang, and X. Yang Zhou, "Negative reflection and negative surface wave conversion from obliquely incident electromagnetic waves," Light: Sci. Appl. **7**(5), 18008 (2018).
21. S. Liu and T. J. Cui, "Flexible controls of scattering clouds using coding metasurfaces," Sci. Rep. **6**(1), 37545 (2016).
22. S. Liu and T. J. Cui, "Concepts, working principles, and applications of coding and programmable metamaterials," Adv. Opt. Mater. **5**(22), 1700624 (2017).